

## Optogenetic control of migration of contractile cells predicted by an active gel model

Oliver M. Drozdowski <sup>1,2</sup>, Falko Ziebert <sup>1,2</sup> & Ulrich S. Schwarz <sup>1,2</sup> 

Cell crawling on flat substrates stems from intracellular flows of the actin cytoskeleton that are driven by both actin polymerization at the front and myosin contractility at the back. Optogenetics makes it experimentally possible to spatially control contraction and possibly cell migration too. Here we theoretically analyze this situation using a one-dimensional active gel model that reflects the property of myosin II to assemble into minifilaments. Our model predicts bistability between sessile and motile solutions when cell adhesion and contractility are sufficiently large and in balance. We show that one can switch between the different states at realistic parameter values via optogenetic activation or inhibition of contractility, in agreement with recent experiments performed for neutrophils in microchannels. We predict the required activation strengths and initiation times, compare the effects of local and global increases of myosin II levels, and show that actin polymerization alone can affect a switch in direction only at high strength.

<sup>1</sup>Institute for Theoretical Physics, Heidelberg University, Philosophenweg 19, 69120 Heidelberg, Germany. <sup>2</sup>BioQuant, Heidelberg University, Im Neuenheimer Feld 267, 69120 Heidelberg, Germany. ✉email: [schwarz@thphys.uni-heidelberg.de](mailto:schwarz@thphys.uni-heidelberg.de)

Crawling migration is an essential property of animal cells and plays a crucial role in development, wound healing, immune response and cancer metastasis<sup>1</sup>. In addition, the design of synthetic cellular systems calls for a better understanding of the minimal components required for cell motility<sup>2</sup>. Obviously the most essential element of cell migration is the symmetry break between front and back. In mesenchymal cell migration, the front uses actin polymerization to push the membrane forward, while the back uses myosin II contractility to generate retrograde flow and to pull the rear forward. Traditionally, these processes are considered to be coordinated by gradients in biochemical activity, most prominently the antagonistic signaling pathways of Rac/Cdc42 and RhoA for front and back, respectively<sup>3</sup>.

A striking feature of locomoting cells is the bistability of their motility behavior: sessile cells can be forced into migration by the application of physical stimuli if the applied stimulus is sufficiently large to polarize their cytoskeleton<sup>4,5</sup>. While on two-dimensional substrates bistability can result from cell shape changes<sup>5,6</sup>, in one-dimensional situations like migration on fibers, lines or channels, bistability has to be mediated by internal polarization. Recently it has been shown for sessile mesenchymal cells on micropatterned lines of fibronectin that polarization can be induced by optogenetic activation of contractility, which leads to rupture of the adhesion sites on the activated side of the cell<sup>7</sup>. More recently, it has been shown that the direction of cell crawling in channels can be reversed by optogenetic stimulation that effectively decreases myosin II contraction at the back<sup>8</sup>. Both experimental setups are essentially one-dimensional, but the second one is even more reduced because it does not rely on changes in cell adhesion. Optogenetic perturbations of cell contractility have revealed that contractile cells usually do not work at saturation, but at an intermediate setpoint of tension that allows for up- and downregulation<sup>7–11</sup>. These observations made with the help of optogenetics shed new light on a long-standing question in the fundamental understanding of cell migration, namely how cell migration works and can be controlled in purely contractile cells. However, it is not clear yet how much further the new tool of optogenetics can be pushed to control cell migration. Moreover it is an open question how much migration control by contractility can be achieved by local versus global means. While the RhoA-pathway is known to generate local increases in

contractility<sup>9</sup>, also global myosin recruitment has been observed to initiate motility, e.g., as a response to nuclear deformation<sup>12,13</sup>. Which mechanism serves which purpose remains puzzling.

The natural framework to understand cytoskeletal flow within cells and the role of contraction is active gel theory<sup>14,15</sup>, which has been used early on to describe cell migration<sup>16</sup>. Despite recent advances in modeling polarization-driven motility with a focus on the role of the stick-slip dynamics of cell adhesion<sup>7,17–19</sup>, an active gel theory that allows one to predict the exact conditions to switch cell migration by manipulation of its internal actin flows is still missing. In contrast to modeling amoeboidal cell migration, for mesenchymal cell migration myosin contractility and not actin polymerization should be the main focus of such a theory. Previous attempts with active gel theory have relied on the assumption that the contractile active stress as a function of motor concentration can be in the saturated regime<sup>20,21</sup>, which however does not agree with the recent experimental finding that usually further contractility can be achieved by optogenetic activation<sup>7–11</sup>.

Here we show that active gel theory can explain and predict optogenetic control of mesenchymal cell migration if one starts from the observation that myosin II molecules assemble into larger complexes. While earlier works used an ideal gas description for the myosins<sup>20,21</sup>, here we describe them as a supercritical van der Waals (vdW) fluid, a concept suggested before for other protein systems<sup>22</sup>. In the myosin context, it accounts both for the crowdedness of the cytosol and the aggregation of myosin II into so-called minifilaments, which are supramolecular clusters that lead to persistent contraction of the actin cytoskeleton. The vdW-model for myosin results in other nonlinearities than the saturation model, but is consistent concerning linear irreversible thermodynamics, since the driving force, the gradient in chemical potential, is still in linear order. Here we introduce the vdW-model into active gel theory from microscopic rules for the binding kinetics of myosin II motors to actin filaments. This model yields an effective diffusion constant that depends on myosin concentration in a nonlinear fashion. We next show that the same function results from linear irreversible thermodynamics for a vdW-fluid in solution. We then show that our vdW-model explains the experimentally observed bistability in cell migration, and that it predicts optogenetic switching between sessile and motile solutions (Fig. 1a). We also parametrize our

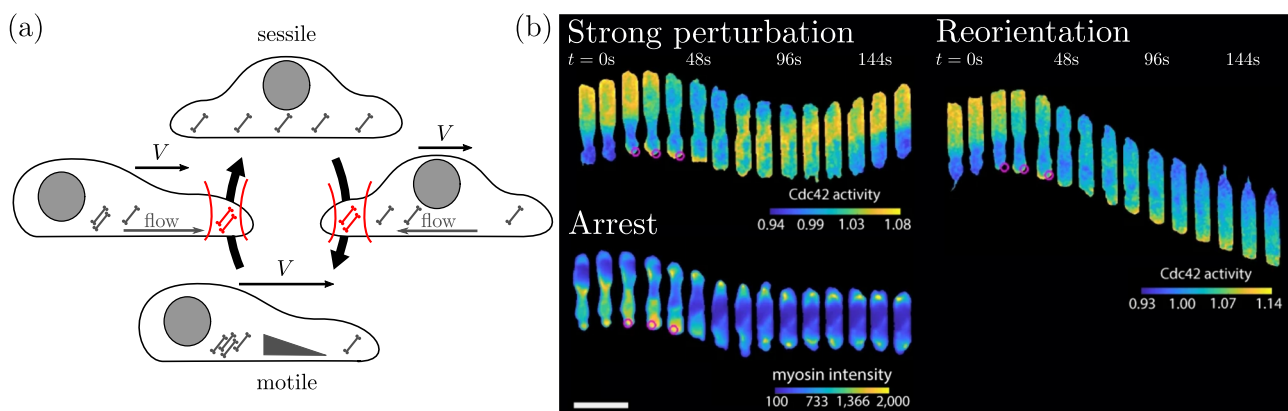


**Fig. 1** Crawling of mesenchymal cells depends strongly on the spatial distribution of myosin motors and can be controlled via optogenetics. **a** A homogeneous motor distribution does not induce intracellular flows and therefore corresponds to a sessile cell (top). In contrast, a myosin gradient corresponds to a motile cell with velocity  $V$  (bottom). Optogenetic activation of contractility (red) can be used to switch between these two states by inducing internal flows (gray arrows). **b** Optogenetic experiments that indirectly affect the myosin system have demonstrated that one-dimensional cell migration in microchannels can be perturbed, arrested and reoriented. Color maps either show front polarity signaling via Cdc42 (perturbation and reorientation) or myosin intensity (arrest). Scale bar is 25  $\mu\text{m}$ . Circles indicate optogenetic activation. Modified under Creative Commons Attribution 4.0 International License from Hadjithodorou et al.<sup>8</sup>.

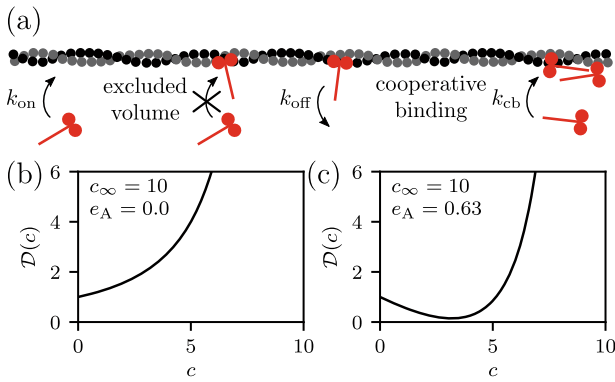


**Fig. 2 Myosin binding kinetics yield nonlinear diffusion in agreement with the van der Waals model.** **a** Microscopic model of myosin (red) un/binding from actin (gray), which leads to a nonlinear diffusion coefficient, corresponding to the van der Waals (vdW) model. We assume that diffusing motors bind with binding rate  $k_{\text{on}}$ , subject to excluded volume effects, and unbind with rate  $k_{\text{off}}$ . We also assume weak cooperative binding with coefficient  $k_{\text{cb}}$ . **b, c** Nonlinear diffusion coefficient  $\mathcal{D}(c)$  of the myosins as a function of their concentration with  $c_{\infty} = 10$  for different intermolecular attraction energies  $e_A$ . **b** Only excluded volume effects (Tonks gas),  $e_A = 0$ . **c** Including attraction (vdW-fluid),  $e_A = 0.63$ .

model and demonstrate that our predictions agree with the recent experiments on motility reorientation and suggest possible alternative protocols to achieve experimental control of cell migration. In particular, our model is able to describe the experimentally observed phenomena of motility perturbation, arrest and reorientation as a function of cell contractility (Fig. 1b)<sup>8</sup>. In addition, we compare the effect of local versus global myosin recruitment. We find that localized and reversible contractility increases allow for full controllability, while global myosin recruitment is less versatile, but nevertheless achieves robust motility initiation. These findings reconcile previous experimental observations that motility can be initiated both via local patterning<sup>7,23</sup>, in the form of contractility gradients in cell migration, as well as via global recruitment, e.g., as a reaction to nuclear deformation<sup>12</sup>. We also implement actin polymerization and find that it can effect motility reversal and inversion of the myosin gradient only at very high levels, which further underscores the central role of contractility.

## Results

**Active gel model.** Cells in microchannels are effectively one-dimensional. Following the usual approach for a minimal version of active gel theory, we model them with the constitutive relation of an infinitely compressible active gel with a linear dependence of the active stress on the myosin concentration field  $c(x, t)$ :

$$\eta \partial_x v(x, t) = \sigma(x, t) - \chi c(x, t). \quad (1)$$

Here  $v(x, t)$  is the flow velocity field,  $\eta$  the shear viscosity,  $\sigma(x, t)$  the total stress field and  $\chi$  the contractility per motor protein. We assume viscous drag with the substrate,  $\partial_x \sigma(x, t) = \xi v(x, t)$ , with a friction coefficient  $\xi$ . Because our focus here is on contractility and not on adhesion, we refrain from including any heterogeneity in friction. The cell is considered to have a variable length, with left edge  $l_-(t)$  and right edge  $l_+(t)$ , and an elastic boundary condition  $\sigma(l_{\pm}, t) = -k(L(t) - L_0)/L_0$ , where  $L(t) = l_+(t) - l_-(t)$  is the cell length and  $L_0$  its reference length. This constraint reflects cellular volume homeostasis, which in cells is achieved mainly by hydrostatic and osmotic pressure control, and assumes instantaneous communication between the front and the back, which can be provided by membrane tension. In the absence of any other

effects, the flow field determines the movement of the boundaries,  $v(l_{\pm}, t) = \dot{l}_{\pm}(t)$ . In the presence of polymerization at the cell boundaries, we have  $v(l_{\pm}, t) = \dot{l}_{\pm}(t) + v_p^{\pm}$  with fixed polymerization velocities  $v_p^{\pm}$  (compare Drozdowski et al.<sup>24</sup>).

**Microscopic model.** We now turn to the main focus of this work, namely the effect of myosin contractility. Its optogenetic activation through the Rho-pathway leads to both assembly of myosin II minifilaments and force generation by their motorheads, resulting in the motor stress  $\chi c(x, t)$ . Because the minifilaments have a finite size around 300 nm and cannot directly touch each other due to the requirement of an organized actin network around them, the assembly process cannot proceed without limits. Moreover it is very dynamic, with myosin molecules continuously exchanging between solution and minifilaments, as verified by experiments with fluorescence recovery after photobleaching<sup>25</sup>.

We first show that a microscopic model of these processes leads to a nonlinear concentration-dependent diffusion constant  $D(c)$ . We consider a two-species model of bound and diffusing myosin motor proteins (Fig. 2a), with concentrations  $c(x, t)$  and  $c_d(x, t)$ , respectively, similarly to previous active gel models with myosins<sup>26</sup>. The bound motors are passively advected with the active gel with the flow velocity  $v(x, t)$ , while the unbound motors diffuse freely. The un/binding process is described by a (in general nonlinear) binding kinetics  $R(c, c_d)$ , yielding:

$$\begin{aligned} \partial_t c(x, t) + \partial_x(v(x, t) c(x, t)) &= R(c, c_d), \\ \partial_t c_d(x, t) - \tilde{D} \partial_x^2 c_d(x, t) &= -R(c, c_d), \end{aligned} \quad (2)$$

with  $\tilde{D}$  being the diffusion coefficient of the unbound myosins. For the binding kinetics, we assume:

$$R(c, c_d) = \frac{k_{\text{on}}}{c_{\infty}} (c_{\infty} - c) c_d - k_{\text{off}} c + \frac{k_{\text{cb}}}{c_{\infty}^2} (c_{\infty} - c)^2 c c_d, \quad (3)$$

describing binding, unbinding, and cooperative binding, respectively. Here  $k_{\text{off}}$  is the linear unbinding rate. The excluded volume effect introduces a factor of  $(c_{\infty} - c)/c_{\infty}$  to the binding rate, which models that a free space on the actin filament is needed. For the cooperative binding this term is squared as it includes both the probability for a diffusing motor to find a free binding space and for a cooperative binding partner to be next to such a binding space. The cooperativity is considered via a term  $\propto c c_d$ , describing the binding of an unbound motor due to binding to an already bound motor, thus modeling the growth of a myosin II minifilament. Note that in the dilute limit, i.e., for small  $c/c_{\infty}$ , the binding rate is given by  $k_{\text{on}}$  and the cooperative binding coefficient by  $k_{\text{cb}}$ .

Assuming (local) chemical equilibrium,  $R(c, c_d) = 0$ , and introducing the linear reaction constant  $K = k_{\text{on}}/k_{\text{off}}$  and the relative cooperative binding ratio  $e_A = 2k_{\text{cb}}/k_{\text{on}}$ , we obtain for the equilibrium concentration:

$$\begin{aligned} c_d &= \frac{1}{K} \frac{c c_{\infty}}{c_{\infty} - c} \frac{1}{1 + (e_A/2c_{\infty})(c_{\infty} - c)c} \\ &\approx \frac{1}{K} \left( \frac{c c_{\infty}}{c_{\infty} - c} - \frac{e_A}{2} c^2 \right), \end{aligned} \quad (4)$$

where we assumed weak cooperativity in order to use a Taylor approximation. Inserting this result into the sum of the equations for  $c$  and  $c_d$ , Eq. (2), i.e., assuming local chemical equilibrium, and then taking the limit of fast binding  $K \rightarrow \infty$  and fast diffusion  $\tilde{D}/K \rightarrow D$  (similarly to previous microscopic models<sup>26</sup>) yields a single advection-diffusion equation for the bound motors,

namely:

$$\partial_t c = -\partial_x(\nu c) + \partial_x(D(c)\partial_x c), \quad (5)$$

with a nonlinear concentration-dependent diffusion coefficient:

$$D(c) = DD(c) = D \left[ \left( 1 + \frac{c}{c_\infty - c} \right)^2 - e_A c \right]. \quad (6)$$

We note that the effects of such concentration-dependent diffusion coefficients have been observed experimentally<sup>27</sup>, for instance in the context of binary liquids<sup>28</sup> and colloidal suspensions of hard spheres<sup>29</sup>. It has been used in models for bacterial growth<sup>30</sup> and very recently also for excluded volume effects of myosins in cells<sup>31</sup>. Inhomogeneous myosin diffusion coefficients in the cell have been reported in fibroblasts<sup>32</sup>.

**Myosins as van der Waals fluid.** Next, we show that the nonlinear diffusion constant arising from the microscopic model corresponds to the linear irreversible thermodynamics of a van der Waals (vdW) fluid. We start with the chemical potential  $\mu_c$  of the vdW-fluid<sup>33</sup>:

$$\mu_c = -N_A k_B T \log \left( \frac{1/N_A - cb}{cb} \right) + N_A k_B T \frac{cb}{1/N_A - cb} - 2aN_A^2 c + N_A k_B T \log \left( \lambda_{th}^{3/2} \right). \quad (7)$$

Here  $N_A$  is the Avogadro number,  $k_B$  the Boltzmann constant,  $T$  temperature,  $b$  the vdW excluded volume and  $a$  the average value of the attractive interaction energy per unit concentration.  $\lambda_{th} = (2\pi\hbar^2/mk_B T)$  is the thermal wavelength. According to linear irreversible thermodynamics<sup>34</sup>, the diffusive particle flux  $J_D$  follows from the gradient of the chemical potential,  $J_D \propto \partial_x \mu$ . The diffusive part of the continuity equation  $\partial_t c = -\partial_x J_D$  then yields a diffusion equation with the same diffusion coefficient  $D(c)$  as derived above on microscopic ground (Eq. (6)), when we identify the saturation concentration  $c_\infty = 1/N_A b$  and the attractive energy  $e_A = 2aN_A/k_B T$ . Including only volume exclusion for the binding in the microscopic model, one obtains the nonlinear diffusion coefficient of the so-called *Tonks gas* (with excluded volume, but  $e_A = 0$ ). This shows that the excluded volume concentration  $c_\infty$  of the vdW-model describes the steric constraints on the actin filaments. In Fig. 2b, c, we plot  $D(c)$  from Eq. (6) without and with attractive energy  $e_A$ , respectively (the first case corresponds to the Tonks gas). In both cases, one sees the singularity for  $c = c_\infty$ , which results from hard core repulsion and increased diffusion at high concentrations. The energetic term leads to a slowdown of diffusion for intermediate concentrations.

**Full model.** Our full model is defined by combining the constitutive active gel equation for  $\nu$  from Eq. (1), the advection-diffusion equation for myosin concentration  $c$  from Eq. (5) and the nonlinear diffusion constant  $D(c)$  from Eq. (6) corresponding to the vdW-fluid. For the advection-diffusion equation, we consider no-flux boundary conditions at the edges, i.e.,  $\partial_x c(l_\pm, t) = 0$ . Following earlier work along these lines<sup>20,24</sup>, we non-dimensionalize length by  $L_0$ , time by  $L_0^2/D$ , stress by  $k$ , and concentration by  $c_0 = \int c dx/L_0$ . We then map the problem on the interval  $[0, 1]$  using  $u = (x - l_-)/L$  and get three dimensionless model parameters: the length ratio  $\mathcal{L} = \sqrt{\eta/(\xi L_0^2)}$  arising from the competition between viscous and frictional dissipation; the Péclet number  $Pe = k/\xi D$  describing the importance of advection versus diffusion; and myosin contractility  $\mathcal{P} = \chi c_0/k$ . The inverse Péclet number  $\mathcal{A} = 1/Pe$  can also be interpreted as adhesion strength, because a large value of  $\mathcal{A}$  corresponds to strong friction if  $\mathcal{L}^2 \mathcal{A} = D\eta/kL_0^2$  is kept fixed, which is a combination of

quantities that typically cannot be changed in experiments. In the following, adhesiveness  $\mathcal{A}$  and contractility  $\mathcal{P}$  are considered as the main parameters, as experimentally they are known to control transitions in cell state.

Defining the cell center  $G = (l_+ + l_-)/2$  and the advection velocity  $\hat{\nu}(u) = -\dot{G} + \dot{L}(1/2 - u)$ , and rescaling  $\tilde{c} = Lc$ , we finally arrive at our central equations, namely the following boundary value problem (BVP):

$$\begin{aligned} \mathcal{L}^2/L^2 \partial_u^2 \sigma - \sigma &= -\mathcal{P}/L \tilde{c}, \\ \partial_t \tilde{c} + \frac{1}{L} \partial_u \left[ \left( \frac{1}{\mathcal{A}L} \partial_u \sigma + \hat{\nu} \right) \tilde{c} \right] &= \frac{1}{L^2} \partial_u [D(\tilde{c}/L) \partial_u \tilde{c}], \end{aligned} \quad (8)$$

with the boundary conditions  $\sigma(u_\pm, t) = -(L(t) - 1)$  and  $\partial_u c(u_\pm, t) = 0$  with  $u_- = 0$ ,  $u_+ = 1$ . As we will show below, this system can be comprehensively analyzed using a combination of analytical and numerical methods.

The parameters of the model can be estimated from experimental data for crawling cells. Following earlier work<sup>24</sup>, one obtains  $\mathcal{L}^2 = 1.25$  and  $\mathcal{P} = 0.1$ .  $\mathcal{A}$  can be determined from  $k = 10^4$  Pa<sup>20,24,35,36</sup>,  $\xi = 2 \cdot 10^{14}$  Pa s/m<sup>24,37</sup> and  $D = 0.7 \cdot 10^{-12}$  m<sup>2</sup>/s<sup>32,37-39</sup> to be  $\mathcal{A} \approx 1/70$ , we choose  $\mathcal{A} = 1/77$  (details on parameters given in Supplementary Information (SI) Table S1). Concerning the vdW-parameters, we limit our discussion to the supercritical vdW-fluid<sup>33</sup>, i.e., the temperature is above the critical temperature  $k_B T_c = 8a/27b$ , corresponding to attractive energies  $e_A < e_A^{(c)} = 27/4c_\infty$ . This supercriticality implies the coexistence of motor protein clusters of different sizes without strict phase separation, very much resembling the situation in the cell. Myosin motors have a coiled coil with length  $\approx 150$  nm, two head domains of size  $\approx 7$  nm<sup>40</sup> and the myosin concentration in cells is of the order of  $c_0 \approx \mu M$ <sup>41</sup>. A rough estimate for the volume of one (unclustered) myosin motor is thus  $10^2$  nm<sup>2</sup> · 100 nm. This implies the estimate  $c_\infty = 100$ , not accounting, however, for crowding in the cell or finite thickness of the cortex, which should decrease this number. In the microscopic motivation of the vdW-fluid, the saturation concentration  $c_\infty$  describes the concentration maximum of bound motors to the actin network, also justifying a smaller  $c_\infty$  value. Therefore we use  $c_\infty = 10$ , which implies  $e_A^{(c)} = 0.675$ . This saturation concentration is consistent to the experimental situation. According to our model, a fully saturated, motile and polarized cell has a myosin-enriched region at the back with a fraction of  $1/Lc_\infty \approx 9\%$  of the cell length. From experiments, one can estimate a fraction of 20–40%<sup>8,20</sup>, implying a lower boundary of  $c_\infty \gtrsim 4$ . In practice, the saturation concentration should be larger, as steady state profiles are expected to not be so strongly saturated. Note that for the vdW-fluid  $e_A = 20\pi e_{min}/9c_\infty \approx 0.7 \cdot e_{min}$ , with  $e_{min}$  being the binding energy in the Lennard-Jones potential of the vdW-fluid (in units of  $k_B T$ ). While  $e_A$  could be obtained from microscopic considerations, we choose  $e_A = 0.63$ , for which bistability occurs for the parameters used within the study. This value is within the supercritical parameter region, consistent with the assumption of weak cooperativity, and is close to the thermal energy scale  $k_B T$ , reflecting the dynamic nature of the system.

**Bistability between sessile and motile solutions.** We will now discuss how the effective nonlinear diffusion arising from volume exclusion and aggregation of myosin results in bistability between sessile and motile solutions. Our focus will be on the case without polymerization, which we will discuss only in the end, thus  $v_p^\pm = 0$  for the time being. To find the steady states, one assumes  $\dot{l}_\pm = V$ , with velocity  $V$ ,  $\dot{L} = 0$  and steady profiles. One then obtains two coupled ordinary differential equations. The case  $D(c) \equiv 1$  has already been studied in refs. 42,43: two non-motile solution families exist with flat stress profiles  $\sigma \equiv -(L - 1)$  and

lengths  $\hat{L}_\pm = (1 \pm \sqrt{1 - 4\mathcal{P}})/2$ . More complex solutions bifurcate from these branches. However, only two were found to be asymptotically stable, the trivial branch  $\hat{L}_+$  and a motile branch bifurcating from it, with a peak in the motor concentration at the trailing edge<sup>42</sup>.

For the nonlinear diffusion considered here, a flat stress profile is still a steady state solution. In the following we focus on the bifurcation from the sessile, flat-stress state ( $L = \hat{L}_+$ ,  $\sigma = 1 - \hat{L}_+$ ,  $\hat{c} = 1/\hat{L}_+$ ) to the first motile state, as our numerical results suggest that these are again the only stable solutions for experimentally relevant parameters. Figure 3a shows the results from the continuation in  $Pe$  for cell length and velocity. We see that approaching the critical  $e_A^{(c)}$  from below renders the supercritical pitchfork bifurcation toward the motile solution to be subcritical, implying bistability. Analytically obtained bifurcation points (indicated as circles) are discussed in Supplementary Note 1 and agree with the numerics, showing that increasing the attraction  $e_A$  in addition decreases the value of  $Pe$  at which the bifurcation occurs. Hence, attractive interactions both induce bistability and reduce the motility threshold. We stress that for pure volume exclusion (Tonks gas) no bistability is obtained. A detailed comparison to other proposed models is given in Supplementary Note 2, where we identify the minimal

components in nonlinear diffusion necessary for bistability. We find that at least a quadratic contribution of  $c$  in  $\mathcal{D}(c)$  is necessary where positive higher order terms are neglected compared to the Tonks gas. This is in line with our interpretation of a slow-down of diffusion compared to exclusion via the chemical potential (cf. SI, Fig. S3). We also investigated the full, time-dependent BVP numerically, using the discontinuous Galerkin finite elements method<sup>44,45</sup> (see Methods section), and found that indeed both solutions marked in Fig. 3a as solid curves are stable in the bistable regime (cf. SI, Fig. S1).

Using advanced continuation methods (branch point and fold continuation<sup>46</sup>, see Methods section), we determined the boundaries of the three different regimes—sessile, bistable and motile—as shown by the state diagram in Fig. 3b. Note that we now kept  $\mathcal{L}^2\mathcal{A}$  fixed as explained above. In Fig. 3b, we focused on the range around the experimentally reasonable values  $\mathcal{P} \approx 0.1$  and  $\mathcal{A} \approx 1/77$  (a full diagram can be found in the SI, Fig. S2). We see that bistability requires a balance between adhesion and contractility. Starting in the bistable regime, increasing adhesion leads to a transition to the non-motile state, while increasing contractility favors the motile regime. Already a change in contractility of 5% allows for these transitions. Note that changing  $e_A$  shifts all the boundaries and hence, depending on  $e_A$ , also the opposite scenario can occur, i.e., decreasing adhesion inducing motility.

Finally, Fig. 3c shows the normalized motor concentrations  $c(u)L$  of the three possible states in the coexistence region. The unstable branch displays enrichment of motors at the trailing edge, while the motile branch develops a layer of high myosin concentration. Importantly, the volume exclusion of the vdW limits the height of the concentration (and stress) peak at the edges even for small  $\mathcal{A}$  (cf. SI, Fig. S1e). This has to be contrasted to the linear model, where unrealistically large peaks develop<sup>20</sup>. There a strong myosin peak forms at the trailing edge of a motile cell, which can reach values of up to  $\approx 40$  times the average concentration, completely depleting myosin at the front. In contrast, our model is in agreement with experimental findings of moderate myosin enrichment in the back<sup>47</sup>. The flow profiles  $\dot{u}$  shown in Fig. 3c indicate the flow to the trailing edge. The flow velocity is maximum in the motor-enriched boundary region. Such a local maximum in flow velocity at the edge of the myosin layer is consistent with flow profiles in keratocytes<sup>48</sup>. This, together with the attraction and subsequent minimum diffusion, promotes the formation of the myosin layer. The diffusion coefficient within the cell corresponding to the stable motile case, depicted in Fig. 3c, shows exactly this slowdown at the edge of the myosin-enriched layer. In particular, the diffusion is considerably slower in the back and thus the slowdown of diffusion by clustering effects facilitates bistability.

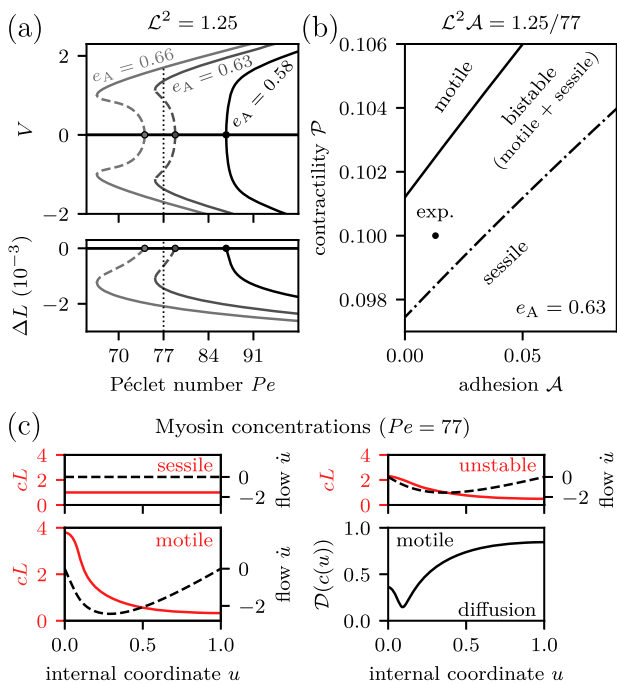


**Fig. 3 Active gel model predicts bistability of cell migration.** **a** Cell velocities  $V$  and the length differences from the sessile state,  $\Delta L = L - \hat{L}_+$ , for the obtained solution branches as a function of Péclet number  $Pe$  for different (supercritical) attractive energies  $e_A$ . The bifurcation points are marked with circles. Stable (unstable) solutions are shown as solid (dashed). **b** State diagram for  $e_A = 0.63$  and for  $\mathcal{L}^2\mathcal{A} = 1.25/77$  fixed (containing parameters, which cannot be changed by the cell, cf. text). Depending on adhesion strength  $\mathcal{A}$  and contractility  $\mathcal{P}$ , one finds a sessile, bistable or motile regime. Parameter values estimated from experiments are marked with a circle and used in **(c)**. The solid/dot-dashed curves correspond to the loci of the pitchfork/saddle node bifurcation. **c** Normalized motor concentration profiles for experimental parameters (and  $V \geq 0$ ) in the bistable regime for the stable sessile, the unstable motile and stable motile solutions, shown as solid red curves. The flow velocities are shown as dashed lines. For the stable motile steady state the resulting diffusion coefficient  $\mathcal{D}(c(u))$  inside the cell is shown as solid black curve.

**Optogenetic switch of cell migration.** Having established that the model displays bistability for experimentally realistic parameters, we next ask if optogenetics can be used to switch between the sessile and motile solutions. Optogenetic control of contractility usually exploits light-induced recruitment of a GTP-exchange factor to the cell membrane, which in turn activates the RhoA-pathway and thus leads to an increase in myosin II contractility and localized myosin recruitment<sup>9,10</sup>. The RhoA-pathway is also known to be involved in upregulating the total contractility level through global myosin recruitment and the subsequent onset of motility, for example as a response to nuclear deformation<sup>12,13</sup>. Finally, an alternative way has been described very recently: there a chemotactic signaling pathway was optogenetically activated in neutrophils, which promotes Rac/Cdc42-activity and thus decreases contractility<sup>8</sup>. Although neutrophils in

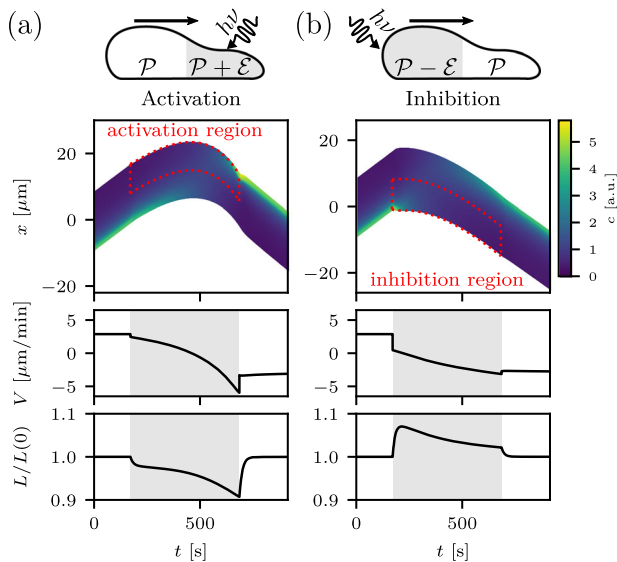


**Fig. 4 Both optogenetic activation and inhibition can reverse cell migration.** **a** Positive activation strength  $\mathcal{E} = 0.07$  at the front and **b** negative activation strength  $\mathcal{E} = -0.07$  at the back both lead to persistent reversal of migration. The upper panels show kymographs, i.e., material cell points as function of time in lab coordinates; myosin concentration is color-coded. The lower panels show cell velocity  $V$  and length  $L$  scaled by initial length  $L(0)$ . Time periods of activation/inhibition are shaded.

general show a mixture of mesenchymal and amoeboidal motility modes, in the context of channel migration they can be considered to be in a mesenchymal motility mode.

Different optogenetic strategies can be implemented in our model by introducing an optogenetic contribution to contraction,  $\mathcal{P} \rightarrow \mathcal{P} + \mathcal{E}\Xi$ , with a shape function  $\Xi$  encoding the spatio-temporal activation and  $\mathcal{E}$  the activation strength<sup>24</sup>.  $\mathcal{E}$  is positive (negative), depending on whether one activates (inhibits) myosin II contractility. We consider a box-shaped function within an activation region  $U_{\text{act}}$ , i.e.,  $\Xi(u, t) = 0$  in general and  $\Xi(u, t) = 1$  only if  $u \in U_{\text{act}}$  and  $t \in [t_{\text{on}}, t_{\text{off}}]$  with turn-on/turn-off times  $t_{\text{on}}$  and  $t_{\text{off}}$ . We first concentrate on the effect of local RhoA activation and local contractility control without a global increase in contractility levels.

Figure 4 shows that both activation in the front half (a) and inhibition in the back half (b) can be used to induce reversals of direction of cell migration. The first protocol has been experimentally shown to achieve reorientation in adhesive situations<sup>7</sup> but has not been analyzed thoroughly with respect to length and velocity changes and full migratory control. However, the simulated trajectories and changes in length for the latter correspond well to the recent experimental results<sup>8</sup>. Note that initiating motility through activation also speaks in favor of contractility saturation not being central in this context.

In the activation protocol the cell’s length decreases as contractility is locally increased. The effect of the perturbation builds up throughout the activation period, since length and velocity are governed by the integrated active stress (see Supplementary Note 3). For the inhibition scenario the effect is opposite, as we inhibit in the half with higher initial concentration: an immediate length response and a more gradual velocity change is obtained. In particular, we predict a decrease of  $|V|$  after turn-off, exactly as observed experimentally<sup>8</sup>.

Focusing on the activation protocol, we next address the question whether optogenetic control of contractility can be used to initiate or arrest motility of cells inside the bistable regime. In

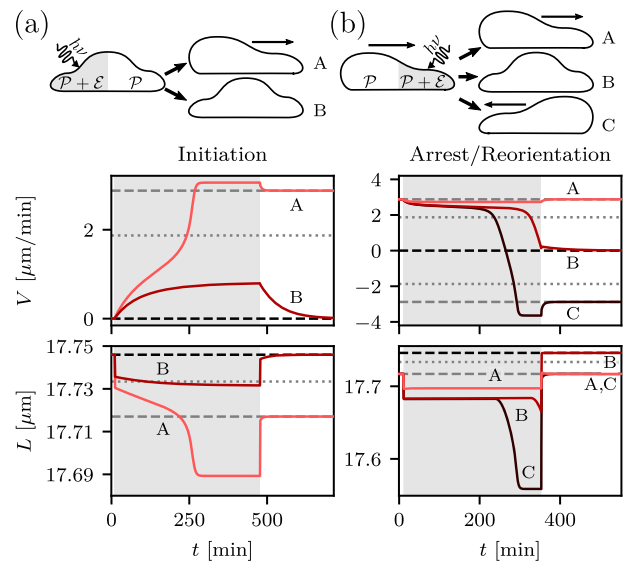


**Fig. 5 Local increase in contractility can both initiate and arrest migration.** **a** Motility can be initiated by optogenetically perturbing the flat motor concentration in (the left) half of the cell; activation  $\mathcal{E}/\mathcal{P} = 1.2\%$ ,  $0.8\%$  for A, B. **b** Motility can be arrested or reoriented when a motile steady state is activated in the leading (right) half; activation  $\mathcal{E}/\mathcal{P} = 6.7\%$ ,  $6.6\%$ ,  $4\%$  for A, B, and C. Solid curves are simulations and dashed (dotted) lines represent stable (unstable) steady states; motile (non-motile) states are in gray (black). Time periods of activation are shaded.

Fig. 5a, we started with the non-motile steady state and activated the left half. Motility is indeed initiated for  $\mathcal{E}$  as small as  $1.2\%$  of  $\mathcal{P}$ . Increasing  $\mathcal{E}$  further leads to faster initiation. For the smaller  $\mathcal{E}$  shown, the perturbation is not sufficiently strong for the induced flow to overcome diffusion and the system cannot leave the basin of attraction of the sessile state. In Fig. 5b, we started with the motile steady state (moving to the right) and activated the right (leading) half. Compared to the case in (a), now larger perturbations are required, because in the motile regime the advection from motility is dominating and has to be overcome. Arrest is possible only when fine-tuning the turn-off of the optogenetic signal: it has to occur in the “re-symmetrized region” that belongs to the basin of attraction of the sessile solution; activating beyond this point rather induces reorientation. Again, larger strengths  $\mathcal{E}$  lead to faster arrest/reorientation.

**Timescale of motility initiation.** Having demonstrated the possibility to initiate or arrest cell migration by optogenetics, we now predict the corresponding time scales. In Fig. 6, we show the time  $t_{\text{ini}}$  at which the steady state velocity is reached. For the relatively weak activation strength considered here, these times vary between hundreds and tens of minutes; later we will see that they can be below minutes for strong activation strength. In general we find that  $t_{\text{ini}}$  is larger for stronger adhesion, as one would expect. Initiation is faster for larger activation strengths, with an asymptotic dependence of  $t_{\text{ini}} \sim (\mathcal{E}/\mathcal{P})^{-1}$ , cf. Fig. 6a. Using continuation of the optogenetically perturbed system (see Supplementary Note 4), we determined the lower initiation boundary for different adhesion strengths, see Fig. 6b. We find that increasing adhesion not only affects the stability of the steady states, but also slows down the dynamics and increases the necessary activation strength. Note that this can be tested experimentally, as activation strength has been shown to depend on the size of the illuminated area and on laser power in optogenetic experiments<sup>9</sup>.

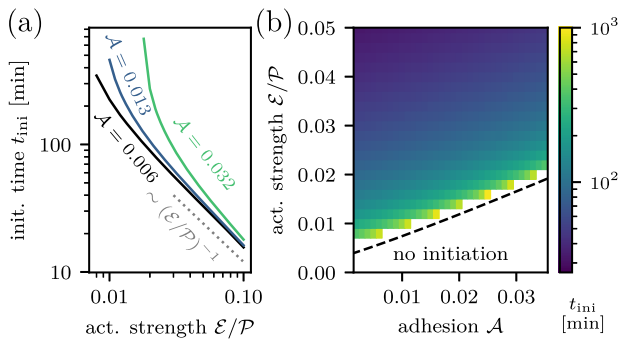


**Fig. 6 Active gel model predicts initiation times.** **a** For different levels of adhesion the initiation time  $t_{\text{ini}}$  for motility differs, where  $A = 0.013$  corresponds to  $\text{Pe} = 77$ . Time  $t_{\text{ini}}$  decreases for larger activations  $\mathcal{E}/\mathcal{P}$ , asymptotically decaying as  $t_{\text{ini}} \sim (\mathcal{E}/\mathcal{P})^{-1}$ . **b** For larger adhesion  $t_{\text{ini}}$  grows larger, with concomitantly increasing minimal activation  $\mathcal{E}/\mathcal{P}$  necessary for motility initiation. The dashed line is the initiation threshold, obtained using continuation.

**Effect of inhibition strength and inhibition time.** To further study the cellular response to the strength and time of perturbations, we next discuss the inhibitory protocol in more detail. Experimental optogenetic perturbations of contraction via inhibition have shown a large variety of possible outcomes when trying to reorient the effectively one-dimensional mode of migration in a microchannel (cf. Fig. 1b)<sup>8,49</sup>. Some cells were not perturbed upon light illumination, while the migratory behavior changed for others. The response ranged from weak response, where the velocity remained positive throughout the experimental observation time; through intermediate response, where the direction changed for a certain amount of time; to strong response with full arrest or reorientation. To recapitulate this behavior, we consider inhibition in the trailing half for  $\varepsilon = -0.04$  and  $-0.09$  for inhibition times of  $\Delta t_{\text{inh}} = 31$  s, 63 s and 126 s. Figure 7 shows that the model predicts all experimentally observed behaviors. To be more realistic, here we use an exponentially plateauing effective temporal activation function  $\Xi^{\text{eff}}$ , which describes the temporal evolution of the contractility following light turn-on and turn-off, as suggested in refs. 9,11,24. The characteristic timescale of de-/activation is assumed to be  $t_{\text{eff}} = 25$  s and the resulting activation is depicted in Fig. 7. We obtain a characteristic dip in the velocity at the end of activation time, resulting from the relaxation of the response function after turn-off. This dip also occurs with a sharp response function on a slower timescale due to relaxation toward the steady state, cf. Fig. 5. In experiments this dip has also been observed on a short timescale<sup>8</sup>, consistent with the relaxation of contraction after turn-off. More precisely, the difference of the largest negative velocity  $V$  at signal turn-off and the final velocity at  $t = 400$  s is of the order of  $\approx 30\%$ , compared to the difference between initial and final velocity in Fig. 7d. In experiments the corresponding relative dip depth was observed to start at 10% in comparable cases, going far beyond in cases with similar final and initial velocities. As in Hadjitheodorou et al.<sup>8</sup>, we also find a change in motility direction before the cell has completely repolarized, i.e., before the myosin motor proteins have accumulated at the new rear.

For intermediate responses to occur (Fig. 7c), the inhibition time has to be too small to achieve full resymmetrization. Weak responses can then result from either even shorter activation times, cf. Fig. 7b, or from smaller inhibition strengths, cf. Fig. 7a. We do not find the slowing down response for large optogenetic inhibition strengths and long times, as the ability to change

the velocity direction induces motor advection, leading to reorientation or arrest on longer time scales. The strong dependence on the inhibition strength could thus explain the variability in experimental outcomes, as cell-to-cell variations in the achievable inhibitions, resulting from the used indirect perturbation of contractility, are likely.

We also investigated the effect of differences in total contractility  $\mathcal{P}$ . In experiments a correlation of weak response to external optogenetic cues and of initial contractility, as well as initial myosin polarization has been found<sup>8</sup>. We performed simulations for different contractilities to find that indeed larger  $\mathcal{P}$  corresponds to a larger myosin peak at the back and faster relaxation toward a motile state (see SI Fig. S5). However, our results indicate that the relative activation strength  $\mathcal{E}/\mathcal{P}$  and activation time determine the strength of the effect on motility. In the bistable regime, which we are most interested in, cf. Fig. 7, the relaxation to the motile steady state is very slow compared to experimental timescales (cf. Fig. 5), due to the competing effect of advection and diffusion. For larger contractilities this relaxation is much faster, but bistability is lost. This suggests that bistability might not be present for all cells.

In all inhibitory protocols cell length has a maximum during inhibition with subsequent relaxation toward the initial length, as the total contractility level has only been modified reversibly with the local protocol. While this general behavior is consistent with experiments, a small length decrease has been found there, which we address next when studying the global myosin recruitment mechanism.

**Effect of global myosin recruitment.** To model global myosin recruitment, we introduce into the model a logistic growth of the concentration upon light illumination, where the saturation concentration is chosen to be  $c_{\infty}$ . Specifically, the equation for the myosin concentration in Eq. (8), is replaced by, in dimensionless form:

$$\partial_t \tilde{c} + \frac{1}{L} \partial_u \left[ \left( \frac{1}{AL} \partial_u \sigma + \hat{v} \right) \tilde{c} \right] = \frac{1}{L^2} \partial_u [\mathcal{D}(\tilde{c}/L) \partial_u \tilde{c}] + (\mathcal{R}/L) \Xi \tilde{c} (Lc_{\infty} - \tilde{c}), \quad (9)$$

where  $\mathcal{R}$  is a non-dimensional myosin recruitment rate. The shape function  $\Xi$  again encodes the spatiotemporal details of the activation protocol. Note that albeit the optogenetic perturbation is local, it yields a global increase of myosin concentration, since the total concentration  $\int \tilde{c} du$  is increased and motors may be advected or diffuse away from the activation region. Here we consider the opposite case from before, i.e., no local increase of contractility ( $\mathcal{E} = 0$ ) beyond the effect of locally added motors. Considering the coupling of  $c$  to the stress, cf. Eq. (8), the increase in the overall myosin level implies identical steady states of the perturbed system compared to an unperturbed system, but with effective contractility parameter  $\mathcal{P}_{\text{eff}} = \mathcal{P} \int_0^1 cL du$  and with changed vdW-parameters:  $c_{\infty} \rightarrow (\mathcal{P}/\mathcal{P}_{\text{eff}})c_{\infty}$  and  $e_A \rightarrow (\mathcal{P}_{\text{eff}}/\mathcal{P})e_A$ .

To approximate the recruitment rate we estimate the time scale of global contractility increase to be bounded from below by  $t_{\text{recr}} \gtrsim 3000$  s, estimated from Oakes et al.<sup>9</sup>. This corresponds to  $\mathcal{R} \lesssim 0.2$ . Figure 8a depicts simulation results for optogenetic perturbations of the nonmotile steady state via the recruitment mechanism. Even for small recruitment rates motility initiation occurs robustly if the activation time is chosen to be sufficiently long, as myosin motor proteins are consistently recruited during activation. This eventually leads to the crossing of the motility threshold in contractility  $\mathcal{P}$  and the sessile steady state becoming unstable (in Fig. 3b, the system moves from the experimental point upwards). Recruitment at the front of a

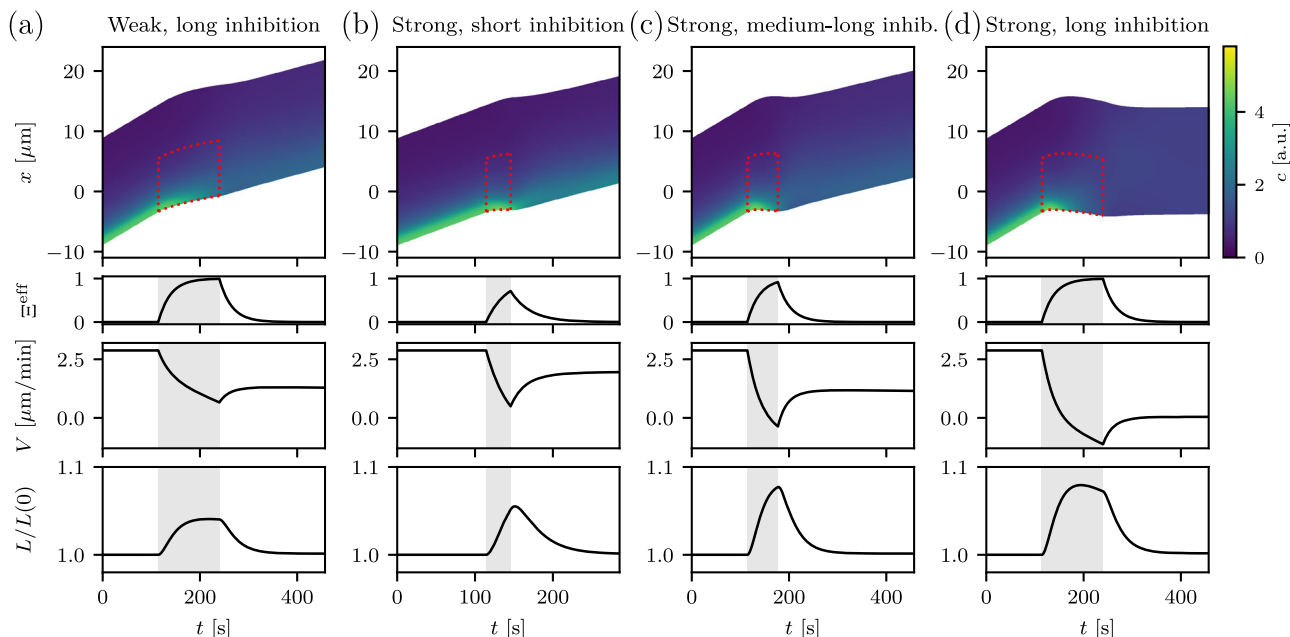


**Fig. 7 Active gel model describes the effects of inhibition strength and inhibition time.** In the upper panels kymographs are shown, i.e., material points as functions of time, of the cell in laboratory coordinates with myosin concentration in color. Below we depict the effective activation of the shape function, caused by the optogenetic signal, as a function of time,  $\Xi^{\text{eff}}$ ; the velocity  $V$ ; and the relative length  $L/L(t=0)$ . The inhibition region is chosen as the left half of the cell, i.e.,  $U_{\text{act}} = [0, 0.5]$ . Time periods of activation are shaded. For a small optogenetic inhibition strength  $\mathcal{E} = -0.04$  (with  $\Delta t_{\text{inh}} = t_{\text{off}} - t_{\text{on}} = 126$  s) **(a)** and for a short inhibition time of  $\Delta t_{\text{inh}} = 31$  s (with  $\mathcal{E} = -0.09$ ) **(b)** only weak motility responses occur. **c** For a strong inhibition ( $\mathcal{E} = -0.09$ ) and an increased  $\Delta t_{\text{inh}} = 63$  s, which is of the order of the experimentally used time, we find a strong motility response: here the velocity becomes negative, even though the initial orientation persists after the signal is turned off. **d** For strong inhibition ( $\mathcal{E} = -0.09$ ) and a longer inhibition time ( $\Delta t_{\text{inh}} = 126$  s), cell migration is arrested.

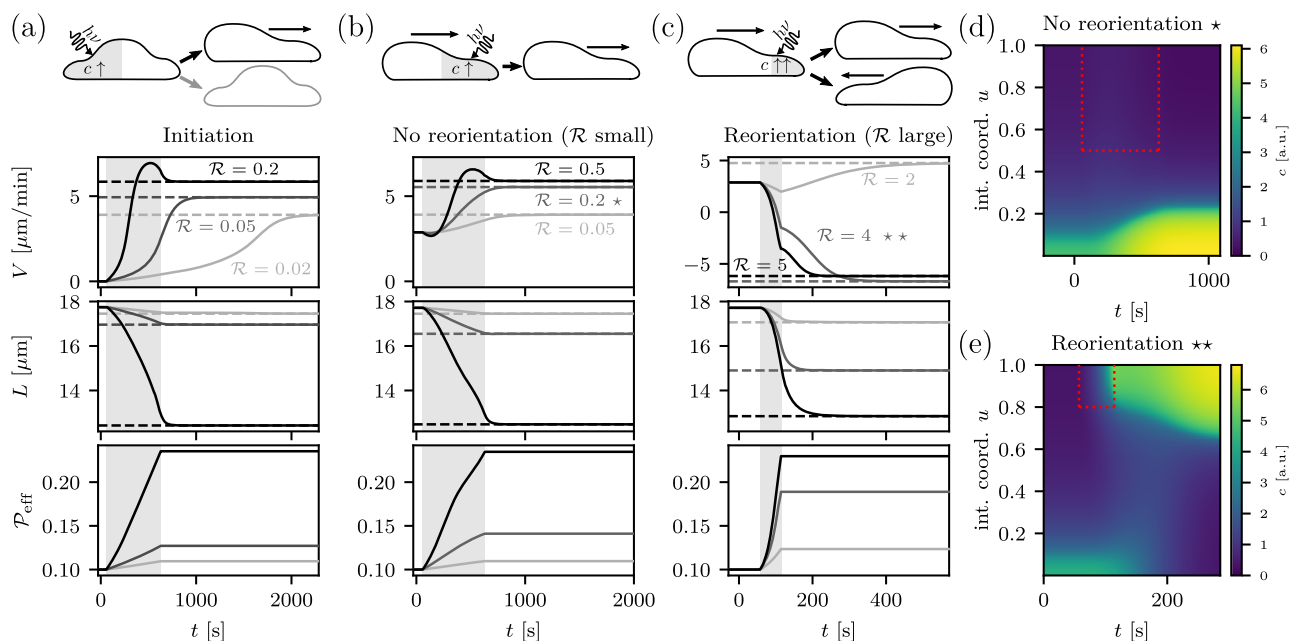


**Fig. 8 Global myosin recruitment initiates motility but does not allow for full control.** **a** Velocity  $V$ , length  $L$  and the effective contractility  $\mathcal{P}_{\text{eff}}$  for activation of the left half  $U_{\text{act}} = [0, 0.5]$  of a sessile state with the recruitment protocol. Motility is initiated robustly, even for small recruitment rates  $\mathcal{R}$ . **b** No reorientation for recruitment in the leading half,  $U_{\text{act}} = [0.5, 1]$ , of a motile cell for small recruitment rates  $\mathcal{R} < 1$ . **c** Reorientation becomes possible for recruitment in the front 20% of the cell,  $U_{\text{act}} = [0.8, 1]$ , with large  $\mathcal{R}$ . The dashed lines in **(a-c)** correspond to the steady state values we expect from the effectively changed vdW-parameters (see text), where  $\mathcal{P}_{\text{eff}}$  is calculated via the integrated final concentration field. Time periods of activation are shaded. **d, e** Kymographs of concentrations in internal coordinates as functions of time for recruitment in the front of motile cells. The dashed lines mark the spatial and temporal extent of the activation region. **d** Kymograph corresponds to the case of no reorientation for  $\mathcal{R} = 0.2$ , marked in **(b)** as  $\star$ . **e** Reorientation for  $\mathcal{R} = 4$ , marked in **(c)** as  $\star\star$ .

motile cell cannot reorient or arrest motility for small (but experimentally realistic) recruitment rates  $\mathcal{R}$ , cf. Fig. 8b. Only increasing  $\mathcal{R}$  allows for reorientation (cf. Fig. 8c), as it is necessary to recruit motors faster than they can be transported to the back by internal flows (cf. Fig. 8d, e). Note that the model only allows for stable steady states with finite length  $L > 0$  for a finite contractility  $\mathcal{P} < 1/4$ , as increasing contractility beyond this point cannot be balanced by the elastic boundary conditions<sup>20</sup>. Therefore increasing  $\mathcal{R}$  means that the activation time has to be shortened to not activate too many myosin motors in the cell. Moreover, we find that reorientation also necessitates the activation of a smaller region at the front to increase the asymmetry and polarize the concentration field into the opposite direction.

Due to the dependence of velocity and length on contractility  $\mathcal{P}$ , we find that recruitment leads to a length decrease, which was also observed experimentally for the inhibitory protocol. As optogenetic activation in the back would not be consistent with reorientation from global recruitment, this shows the secondary role of global recruitment in direction control. This assessment is strengthened by the strong variability in length and velocity after activation with different recruitment rates  $\mathcal{R}$ , which was not observed experimentally<sup>8</sup>. As we expect the recruitment to also depend on the illuminated area, like it was observed for the contractility increase<sup>9</sup>, this should be observable experimentally if global recruitment would be the primary mechanism for motility control.

Figure 8d, e show kymographs of the concentration in internal coordinates for the case of no reorientation (d) and reorientation (e). If the state of motility is not changed, the overall intensity is increased as the total amount of active myosin is increased. This also occurs for reorientation but we also find redistribution of myosin motors to the other edge. This redistribution also occurs after turn-off of the optogenetic recruitment, as the polarization has been switched, leading to overall flow to the other edge. Note that this also occurs for local activation (cf. Fig. 4) and in experiments (cf. Fig. 1b).

To summarize the effect of a global contractility increase through recruitment, full controllability would only be possible for very localized additional recruitment of motor proteins with an unrealistically high recruitment rate. Our model hence strongly suggests that global recruitment is not the primary mechanism for direction control in motility, in agreement with the fact that the RhoA-pathway usually acts locally. Nonetheless global activation can also robustly initiate motility, because it can destabilize the sessile state.

In addition to non-reversible recruitment, also a non-reversible decrease of total contractility could be envisioned. Such a decrease can be implemented by considering a negative recruitment rate  $\mathcal{R} < 0$ . As contractility  $\mathcal{P}$  depends on the integrated concentration, this will eventually lead to a motility arrest, as we effectively move downward in the phase diagram of Fig. 3b. Note that this could be tested experimentally, for example, via myosin degradation due to phototoxicity.

**Reorientation through a switch of polymerization.** We finally turn to the effect of actin polymerization, which mainly occurs at the boundaries, is controlled by Rac/Cdc42 and can also be tuned by optogenetics<sup>50</sup>. As explained above, this effect can be easily incorporated into our model via the boundary conditions, using  $v_p^+ \neq 0$  and  $v_p^- \neq 0$ . Myosin conservation then leads to the modified boundary condition:

$$\partial_u \tilde{c}(u_{\pm}, t) = \frac{[(1/A)\partial_u \sigma(u_{\pm}, t) + L\hat{v}]\tilde{c}(u_{\pm}, t)}{D(\tilde{c}(u_{\pm}, t)/L)}. \quad (10)$$

Here we will assume polymerization at one of the edges without de/polymerization at the corresponding other edge, i.e.,  $v_p^+ > 0$  and  $v_p^- = 0$ , or  $v_p^- < 0$  and  $v_p^+ = 0$ .

We find that such an asymmetric polymerization breaks the symmetry and leads to so-called imperfect bifurcations: the pitchfork bifurcation of the model without polymerization splits into  $2 + 1$  saddle-node bifurcations, see Fig. 9a, b. For large polymerization velocities the bistability is entirely lost as two of the saddle-node bifurcations vanish. To estimate realistic polymerization velocities, we note that in experimental systems, retrograde flow velocities of  $1\text{--}3 \mu\text{m}/\text{min}$  have been measured<sup>51</sup>, which is smaller than single-filament polymerization velocities, being of the order of hundreds of nm per second<sup>52,53</sup>. For experimental cell velocities of  $20 \mu\text{m}/\text{min}$  this entails a lower polymerization velocity boundary of 5% of the cell velocity. In the following we will hence consider  $v_p^+ = 0.05$  (corresponding to  $\approx 4\%$  of the final cell velocity in our simulations) and the stable motile state as the initial state (cf. the red dot at  $Pe = 77$  in Fig. 9a, b). To study the effect of polymerization repolarization, we consider an instantaneous switch to  $v_p^- < 0$  and  $v_p^+ = 0$  from the above steady state.

From the bifurcation diagram in Fig. 9b we find that for small  $|v_p^-|$  a motile steady state without reorientation exists at  $Pe = 77$ . We expect to find a less polarized concentration field which, however, has opposite polarization to the polymerization. Thus the myosin peak is expected to remain at the back with no reorientation ( $V > 0$  prevails). For larger polymerization velocities the saddle-node bifurcation moves past the considered Péclet value and thus the only stable steady state exists at  $V < 0$ , corresponding to a reorientation event. We find for the chosen parameters the critical polymerization value  $|v_p^-| \approx 0.04$ , which is the lower boundary for possible reorientation. To confirm this scenario, we performed dynamical simulations at  $v_p^- = -0.035$  and  $-0.045$  in Fig. 9c, d, respectively. In (b) we find a small myosin layer broadening without reorientation, while in (c) indeed reorientation occurs as the polymerization flow can fully repolarize the myosin field.

We have neglected in this discussion the temporal details of the change in polymerization velocity, but as the existence of the not-reoriented steady state solely depends on the maximum final value of  $|v_p^-|$ , we do not expect dynamical effects to change the scenario. Importantly, note that we find no overshoot in the velocity, contrary to the experimental observations<sup>8</sup>. This suggests that the optogenetic effect on contraction is central in the reorientation experiments. In addition, the magnitude of  $v_p^- \approx -0.04$  suggests that a rather large reversal of the polymerization is necessary to overcome the myosin distribution, with perturbed polymerization velocities comparable to the ones in the motile state. These results again underscore the importance of the contraction effects, which lower this large threshold.

## Discussion

We have shown that active gel theory can explain bistability and optogenetic switching in cell crawling when the myosins perform nonlinear diffusion. We have derived a concentration-dependent diffusion constant  $D(c)$  from a microscopic model for the binding kinetics of the myosins and showed that this result is equivalent to the irreversible thermodynamics approach when the myosins are described as a supercritical vdW-fluid. The model predictions agree well with recent experiments of cell motility inside microchannels<sup>8</sup>, including the time scale of motility arrest and perturbations. The experimental cell velocity and reorientation response are slightly faster than predicted here. However, the time scale of our model is set by the myosin II effective diffusion coefficient  $D$ , which in practice could be larger than for free diffusion. Moreover, in experiments directly perturbing RhoA

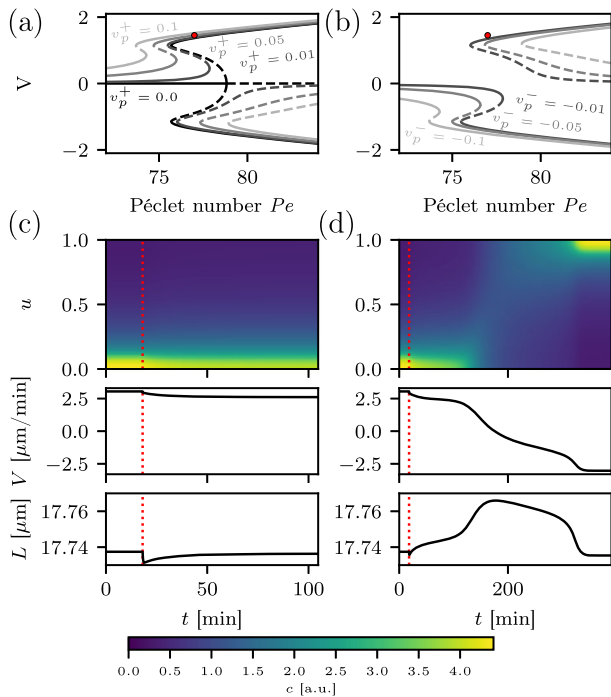


**Fig. 9 Switch of polymerization can lead to reorientation.** Bifurcation diagrams for different polymerization velocities at the right edge  $v_p^+$  with  $v_p^- = 0$  (a) and at the left edge  $v_p^-$  for  $v_p^+ = 0$  (b). The red circle marks the motile steady state velocity for  $v_p^+ = 0.05$ . c Repolarization attempt with a small polymerization velocity  $v_p^- = -0.035$  does not induce motility reorientation. The myosin-enriched layer is spread but no repolarization occurs, as visible in the kymograph of concentration  $c$  in internal coordinates, in the velocity  $V$  and the length  $L$ . The dotted red line marks the time at which instantaneous switching of polymerization occurs. d Repolarization is successful for a larger  $v_p^- = -0.045$ : the polymerization is able to overcome the polarization from myosin motors.

signaling optogenetically, reorientation has been observed to occur on a slower time scale, consistent with our findings<sup>7</sup>. We also find that variations in total contractility lead to faster relaxation for cells in a parameter regime without bistability, consistent with experiments<sup>8</sup>.

Considering the effects of local contractility increase versus global myosin recruitment, we have shown that global recruitment leads to robust motility initiation. This could explain why cells globally upregulate contraction upon nuclear deformation<sup>12</sup>. On the other hand, local contractility increase allows full controllability and thus serves as a robust mechanism to obtain direction control, consistent with the observed myosin distribution in motile cells<sup>23</sup>.

In this work we have estimated reasonable values for the parameters  $c_\infty$  and  $e_A$  that enter the vdW equation of state. While our parametrization rests mainly on observed cellular processes, our microscopic approach also opens the perspective to make direct contact to molecular properties, in particular for reconstituted systems with few components. Especially the choice of  $c_\infty$  as the saturation concentration in the study of recruitment should be reconsidered for simulations of longer activation than considered here. Activating motors until the system is thermodynamically saturated leads to collapse of the model and seems biologically unrealistic. Extending activation into the nonlinear regime of recruitment, which goes beyond the switching scenarios studied here, necessitates a more realistic description of the saturation behavior and also the relaxation toward a homeostatic contractility for long times.

Although not the main focus of this work, our model can easily address the role of actin polymerization by implementing corresponding boundary conditions<sup>24,54</sup>. However, here we demonstrated that myosin contractility is sufficient to explain bistability and switching as experimentally observed. Although migration can also be reoriented by a switch of polymerization direction, this does not fully capture the experimental observations, underlining the importance of contraction in cellular and optogenetic control of motility.

Our work has its main focus on the effect of myosin contractility on internal actin flows and thus does not address the important role of cell adhesion, which is known to also be able to establish cell polarization through contractility, namely through rupture of adhesion sites<sup>7,17–19</sup>. This implies that our predictions are more applicable to experiments that do not depend on adhesion, like cells in microchannels<sup>8,49</sup>, as contrasted to cells on adhesive lines<sup>7</sup>. In order to combine the two research directions in the future in one transparent and minimalistic active gel model, it would be appropriate to formulate a continuum version of the stick-slip dynamics of discrete adhesion bonds. Another direction for future improvements would be the details of the signaling networks controlling myosin contractility and actin polymerization. Combining our active gel model with biochemical repolarization mechanisms on the signaling level could reveal even more modes for optogenetic control of cell migration<sup>55</sup>.

More biological details might be added in the future, but the present work demonstrates that incorporating volume exclusion and attraction in active gel theory is sufficient to identify the fundamental physical processes underlying crawling of contractile cells as long as adhesion is not dominant. We expect that such a fundamental insight will also be very helpful to design synthetic motile cells.

## Methods

**Numerical continuation procedure.** We use AUTO07p<sup>56</sup> for numerical continuation of steady states. To do so, Eq. (8) is transformed into an ordinary differential equation BVP by considering a steady state with  $\dot{t}_+ = \dot{t}_- = V$ . We introduce the auxiliary variable  $s = \sigma + (L - 1)$  for which the boundary conditions read  $s(0) = s(1) = 0$ . The trivial (nonmotile) steady state is then given by  $s \equiv 0$ ,  $V = 0$ ,  $L = (1 + \sqrt{1 - 4\mathcal{P}})/2$ , which we use as starting point for all continuations. Motor conservation introduces the integral constraint  $\int cL du = 1$ .

For Fig. 3a, this solution is continued with principal continuation parameter  $Pe$  and branch switching at the pitchfork bifurcation. For the phase diagram (Fig. 3b), the pitchfork and saddle-node bifurcation loci are continued in the  $(A, \mathcal{P})$  plane for fixed  $L^2A$ . For the study on polymerization, i.e., Fig. 9a, b, first the trivial steady state is continued in  $v_p^\pm$  left and right of the pitchfork bifurcation and then at the desired  $v_p^\pm$  the solution is continued in  $Pe$ . Similarly the steady state with activation is obtained, cf. Fig. S4, and the activation threshold in Fig. 6b is determined via continuation of the corresponding saddle-node bifurcation (see Supplementary Note 4 for details). All simulations are run with a mesh discretization into 20 subintervals with 4 Gauss collocation points each and an adaptive stepsize in the pseudo-arclength continuation.

**Finite element integration method.** The full, time dependent BVP, Eq. (8), was solved with the discontinuous Galerkin (dG) finite elements method, accounting for the heterogeneous diffusion constant via the symmetric weighted interior penalty scheme for the description of the diffusion term<sup>44</sup> and for advection via upwinding. The corresponding weak form is given in Supplementary Note 5. For the interval,  $[0, 1]$ , the mesh was chosen to discretize the interval into  $n_{\text{mesh}} = 100$  equally sized subintervals. The stress  $\sigma$  and the concentration  $\bar{c}$  were solved in a function space with discontinuous Galerkin basis elements of order 2. For the fluxes in the advection-diffusion equation for  $\bar{c}$  the derivatives  $\partial_x \sigma$  were projected into the function space of continuous finite elements of order 1. For the time discretization the time step was chosen to be  $\Delta t = 10^{-3}$  ( $\approx 0.6$  s in real units) for Figs. 5 and 6;  $\Delta t = 10^{-4}$  for Figs. 4, 7–9; and  $\Delta t = 5 \times 10^{-5}$  for the curves in Fig. 8b, c for which the kymographs are plotted. In each time step first the stress equation was solved. Then length and cell center position were integrated via explicit Euler stepping. Finally, the time-dependent equation for  $\bar{c}$  was integrated with an implicit Euler scheme, where the advective flux was computed

from the old stress field. The solver was implemented with FEniCS<sup>45</sup>. The full BVP with optogenetic activation is given in Supplementary Note 3.

### Data availability

All data generated for this study are publicly available at <https://doi.org/10.5281/zenodo.7967125>.

### Code availability

All code written to generate the data shown here is publicly available at <https://doi.org/10.5281/zenodo.7967125>.

Received: 20 October 2022; Accepted: 17 June 2023;

Published online: 30 June 2023

### References

- Bodur, D. L., Pönisch, W., Endres, R. G. & Paluch, E. K. Of cell shapes and motion: the physical basis of animal cell migration. *Dev. Cell* **52**, 550–562 (2020).
- Göpfrich, K., Platzman, I. & Spatz, J. P. Mastering complexity: towards bottom-up construction of multifunctional eukaryotic synthetic cells. *Trends Biotechnol.* **36**, 938–951 (2018).
- Ridley, A. J. et al. Cell migration: integrating signals from front to back. *Science* **302**, 1704–1709 (2003).
- Verkhovskiy, A. B., Svitkina, T. M. & Borisy, G. G. Self-polarization and directional motility of cytoplasm. *Curr. Biol.* **9**, 11–20 (1999).
- Ziebert, F., Swaminathan, S. & Aranson, I. S. Model for self-polarization and motility of keratocyte fragments. *J. R. Soc. Interface* **9**, 1084 (2012).
- Blanch-Mercader, C. & Casademunt, J. Spontaneous motility of actin lamellar fragments. *Phys. Rev. Lett.* **110**, 078102 (2013).
- Hennig, K. et al. Stick-slip dynamics of cell adhesion triggers spontaneous symmetry breaking and directional migration of mesenchymal cells on one-dimensional lines. *Sci. Adv.* **6**, eaau5670 (2020).
- Hadjitheodorou, A. et al. Directional reorientation of migrating neutrophils is limited by suppression of receptor input signaling at the cell rear through myosin II activity. *Nat. Commun.* **12**, 6619 (2021).
- Oakes, P. W. et al. Optogenetic control of RhoA reveals zyxin-mediated elasticity of stress fibres. *Nat. Commun.* **8**, 15817 (2017).
- Valon, L., Marin-Llaurado, A., Wyatt, T., Charras, G. & Trepat, X. Optogenetic control of cellular forces and mechanotransduction. *Nat. Commun.* **8**, 14396 (2017).
- Andersen, T. et al. Cell size and actin architecture determine force generation in optogenetically activated cells. *Biophys. J.* **122**, 684–696 (2023).
- Venturini, V. et al. The nucleus measures shape changes for cellular proprioception to control dynamic cell behavior. *Science* **370**, eaab2644 (2020).
- Lomakin, A. J. et al. The nucleus acts as a ruler tailoring cell responses to spatial constraints. *Science* **370**, eaab2894 (2020).
- Kruse, K., Joanny, J. F., Jülicher, F., Prost, J. & Sekimoto, K. Asters, vortices, and rotating spirals in active gels of polar filaments. *Phys. Rev. Lett.* **92**, 078101 (2004).
- Prost, J., Jülicher, F. & Joanny, J.-F. Active gel physics. *Nat. Phys.* **11**, 111–117 (2015).
- Kruse, K., Joanny, J. F., Jülicher, F. & Prost, J. Contractility and retrograde flow in lamellipodium motion. *Phys. Biol.* **3**, 130 (2006).
- Ron, J. E., Monzo, P., Gauthier, N. C., Voituriez, R. & Gov, N. S. One-dimensional cell motility patterns. *Phys. Rev. Res.* **2**, 033237 (2020).
- Sens, P. Stick-slip model for actin-driven cell protrusions, cell polarization, and crawling. *Proc. Natl Acad. Sci. USA* **117**, 24670–24678 (2020).
- Amiri, B., Heyn, J. C., Schreiber, C., Rädler, J. O. & Falcke, M. On multistability and constitutive relations of cell motion on fibronectin lanes. *Biophys. J.* **122**, 753–766 (2023).
- Recho, P., Putelat, T. & Truskinovsky, L. Mechanics of motility initiation and motility arrest in crawling cells. *J. Mech. Phys. Solids* **84**, 469–505 (2015).
- Lavi, I., Meunier, N., Voituriez, R. & Casademunt, J. Motility and morphodynamics of confined cells. *Phys. Rev. E* **101**, 022404 (2020).
- Wills, P. R. & Winzor, D. J. van der Waals phase transition in protein solutions. *Acta Crystallogr. D.* **61**, 832–836 (2005).
- Mogilner, A., Barnhart, E. L. & Keren, K. Experiment, theory, and the keratocyte: an ode to a simple model for cell motility. *Semin. Cell Dev. Biol.* **100**, 143–151 (2020).
- Drozdowski, O. M., Ziebert, F. & Schwarz, U. S. Optogenetic control of intracellular flows and cell migration: a comprehensive mathematical analysis with a minimal active gel model. *Phys. Rev. E* **104**, 024406 (2021).
- Weissenbruch, K. et al. Distinct roles of nonmuscle myosin II isoforms for establishing tension and elasticity during cell morphodynamics. *Elife* **10**, e71888 (2021).
- Recho, P. & Truskinovsky, L. *Cell Locomotion in One Dimension*, 135–197 (Springer International Publishing, 2016).
- Crank, J. *The Mathematics of Diffusion*. (Clarendon Press, 1975).
- Bardow, A., Göke, V., Koß, H.-J., Lucas, K. & Marquardt, W. Concentration-dependent diffusion coefficients from a single experiment using model-based raman spectroscopy. *Fluid Ph. Equilibria* **228–229**, 357–366 (2005).
- Peppin, S. S. L., Elliott, J. A. W. & Worster, M. G. Solidification of colloidal suspensions. *J. Fluid Mech.* **554**, 147–166 (2006).
- Müller, J. & van Saarloos, W. Morphological instability and dynamics of fronts in bacterial growth models with nonlinear diffusion. *Phys. Rev. E* **65**, 061111 (2002).
- Chelly, H. & Recho, P. Cell motility as an energy minimization process. *Phys. Rev. E* **105**, 064401 (2022).
- Kolega, J. & Taylor, D. L. Gradients in the concentration and assembly of myosin II in living fibroblasts during locomotion and fiber transport. *Mol. Biol. Cell* **4**, 819–836 (1993).
- Johnston, D. *Advances in Thermodynamics of the van der Waals Fluid*. (Morgan & Claypool Publishers, 2014).
- Groot, S. R. D. & Mazur, P. *Non-Equilibrium Thermodynamics*. (Dover Publications, 1984).
- Loosley, A. J. & Tang, J. X. Stick-slip motion and elastic coupling in crawling cells. *Phys. Rev. E* **86**, 031908 (2012).
- Barnhart, E. L., Allen, G. M., Jülicher, F. & Theriot, J. A. Bipedal locomotion in crawling cells. *Biophys. J.* **98**, 933–942 (2010).
- Barnhart, E. L., Lee, K.-C., Keren, K., Mogilner, A. & Theriot, J. A. An adhesion-dependent switch between mechanisms that determine motile cell shape. *PLoS Biol.* **9**, 1–19 (2011).
- Uehara, R. et al. Determinants of myosin II cortical localization during cytokinesis. *Curr. Biol.* **20**, 1080–1085 (2010).
- Luo, T. et al. Understanding the cooperative interaction between myosin II and actin cross-linkers mediated by actin filaments during mechanosensation. *Biophys. J.* **102**, 238–247 (2012).
- McLachlan, A. D. Structural implications of the myosin amino acid sequence. *Annu. Rev. Biophys. Bioeng.* **13**, 167–189 (1984).
- Robinson, D. N., Cavet, G., Warrick, H. M. & Spudich, J. A. Quantitation of the distribution and flux of myosin-II during cytokinesis. *BMC Cell Biol.* **3**, 4 (2002).
- Recho, P., Putelat, T. & Truskinovsky, L. Contraction-driven cell motility. *Phys. Rev. Lett.* **111**, 108102 (2013).
- Bois, J. S., Jülicher, F. & Grill, S. W. Pattern formation in active fluids. *Phys. Rev. Lett.* **106**, 028103 (2011).
- Ern, A., Stephansen, A. F. & Zunino, P. A discontinuous galerkin method with weighted averages for advection-diffusion equations with locally small and anisotropic diffusivity. *IMA J. Numer. Anal.* **29**, 235–256 (2009).
- Alnæs, M. et al. The fenics project version 1.5. *Arch. Numer. Softw.* **3**, 9–23 (2015).
- Doedel, E. J. *Lecture Notes on Numerical Analysis of Nonlinear Equations*, Chap. 1, 1–49 (Springer, 2007).
- Svitkina, T. M., Verkhovskiy, A. B., McQuade, K. M. & Borisy, G. G. Analysis of the actin-myosin II system in fish epidermal keratocytes: mechanism of cell body translocation. *J. Cell. Biol.* **139**, 397 (1997).
- Rubinstein, B., Fournier, M. F., Jacobson, K., Verkhovskiy, A. B. & Mogilner, A. Actin-myosin viscoelastic flow in the keratocyte lamellipod. *Biophys. J.* **97**, 1853–1863 (2009).
- Hadjitheodorou, A. et al. Leading edge competition promotes context-dependent responses to receptor inputs to resolve directional dilemmas in neutrophil migration. *Cell Syst.* **14**, 196–209.e6 (2023).
- Valon, L. et al. Predictive spatiotemporal manipulation of signaling perturbations using optogenetics. *Biophys. J.* **109**, 1785–1797 (2015).
- Valotton, P., Danuser, G., Bohnet, S., Meister, J.-J. & Verkhovskiy, A. B. Tracking retrograde flow in keratocytes: news from the front. *Mol. Biol. Cell* **16**, 1223–1231 (2005).
- Mogilner, A. & Oster, G. Cell motility driven by actin polymerization. *Biophys. J.* **71**, 3030–3045 (1996).
- Mogilner, A. & Oster, G. Force generation by actin polymerization II: the elastic ratchet and tethered filaments. *Biophys. J.* **84**, 1591–1605 (2003).
- Recho, P. & Truskinovsky, L. Asymmetry between pushing and pulling for crawling cells. *Phys. Rev. E* **87**, 022720 (2013).
- Buttenschön, A. & Edelstein-Keshet, L. Cell repolarization: a bifurcation study of spatio-temporal perturbations of polar cells. *Bull. Math. Biol.* **84**, 114 (2022).
- Doedel, E. J. et al. AUTO-07P: continuation and bifurcation software for ordinary differential equations (2007).

## Acknowledgements

This research was conducted within the Max Planck School Matter to Life supported by the German Federal Ministry of Education and Research (BMBF) in collaboration with the Max Planck Society. We also acknowledge support by the Deutsche Forschungsgemeinschaft (DFG, German Research Foundation)—Projektnummer 390978043. For the publication fee we acknowledge financial support by the DFG within the funding programme “Open Access Publikationskosten” as well as by Heidelberg University. U.S.S. is member of the Interdisciplinary Center for Scientific Computing (IWR) at Heidelberg.

## Author contributions

O.M.D., F.Z. and U.S.S. were involved in developing the model. O.M.D. performed the calculations, developed the numerical code and analyzed the data. F.Z. and U.S.S. designed and supervised the research. All authors wrote the paper.

## Funding

Open Access funding enabled and organized by Projekt DEAL.

## Competing interests

The authors declare no competing interests.

## Additional information

**Supplementary information** The online version contains supplementary material available at <https://doi.org/10.1038/s42005-023-01275-0>.

**Correspondence** and requests for materials should be addressed to Ulrich S. Schwarz.

**Peer review information** *Communications Physics* thanks the anonymous reviewers for their contribution to the peer review of this work. A peer review file is available.

**Reprints and permission information** is available at <http://www.nature.com/reprints>

**Publisher's note** Springer Nature remains neutral with regard to jurisdictional claims in published maps and institutional affiliations.



**Open Access** This article is licensed under a Creative Commons Attribution 4.0 International License, which permits use, sharing, adaptation, distribution and reproduction in any medium or format, as long as you give appropriate credit to the original author(s) and the source, provide a link to the Creative Commons license, and indicate if changes were made. The images or other third party material in this article are included in the article's Creative Commons license, unless indicated otherwise in a credit line to the material. If material is not included in the article's Creative Commons license and your intended use is not permitted by statutory regulation or exceeds the permitted use, you will need to obtain permission directly from the copyright holder. To view a copy of this license, visit <http://creativecommons.org/licenses/by/4.0/>.

© The Author(s) 2023